

Data-driven simulation of rapid flux enhancement of energetic electrons with an upper-band whistler burst

Shinji Saito¹, Satoshi Kurita², Yoshizumi Miyoshi³, Satoshi Kasahara⁴, Shoichiro Yokota⁵, Kunihiro Keika⁴, Tomoaki Hori⁶, Yoshiya Kasahara⁷, Shoya Matsuda⁸, Masafumi Shoji⁹, Satoko Nakamura³, Ayako Matsuoka², Shun Imajo⁹, and Iku Shinohara⁸

¹National Institute of Information and Communications Technology

²Kyoto University

³Institute for Space-Earth Environmental Research, Nagoya University

⁴The University of Tokyo

⁵Graduate School of Science, Osaka University

⁶Institute for Space-Earth Environmental Research (ISEE), Nagoya University

⁷Kanazawa University

⁸Japan Aerospace Exploration Agency

⁹Nagoya University

November 23, 2022

Abstract

The temporal variation of the energetic electron flux distribution caused by whistler mode chorus waves through the cyclotron resonant interaction provides crucial information on how electrons are accelerated in the Earth's inner magnetosphere. This study employing a data-driven test-particle simulation demonstrates that the rapid deformation of energetic electron distribution observed by the Arase satellite is not simply explained by a quasi-linear diffusion mechanism, but is essentially caused by nonlinear scattering: the phase trapping and the phase dislocation. In response to upper-band whistler chorus bursts, multiple nonlinear interactions finally achieve an efficient flux enhancement of electrons on a time scale of the chorus burst. A quasi-linear diffusion model tends to underestimate the flux enhancement of energetic electrons as compared with a model based on the realistic dynamic frequency spectrum of whistler waves. It is concluded that the nonlinear phase trapping plays an important role in the rapid flux enhancement of energetic electrons observed by Arase.

Data-driven simulation of rapid flux enhancement of energetic electrons with an upper-band whistler burst

S. Saito¹, S. Kurita², Y. Miyoshi³, S. Kasahara⁴, S. Yokota⁵, K. Keika⁴, T. Hori³, Y. Kasahara⁶, S. Matsuda⁷, M. Shoji³, S. Nakamura³, A. Matsuoka⁸, S. Imajo³, I. Shinohara⁷

¹Space Environment Laboratory, Applied Electromagnetic Research Institute, National Institute of Information and Communications Technology, Tokyo, Japan

²Research Institute for Sustainable Humanosphere, Kyoto University, Uji, Japan

³Institute for Space-Earth Environmental Research, Nagoya University, Nagoya, Japan

⁴Graduate School of Science, University of Tokyo, Tokyo, Japan

⁵Graduate School of Science, Osaka University, Toyonaka, Japan

⁶Graduate School of Natural Science and Technology, Kanazawa University

⁷Institute of Space and Astronautical Science, Japan Aerospace Exploration Agency, Kanagawa, Japan

⁸Graduate School of Science, Kyoto University, Kyoto, Japan

Key Points:

- The data-driven simulation of rapid flux enhancement has been performed using plasma/particle and wave data obtained by Arase.
- The simulation results reproduce the observed temporal variations of energetic electron flux distributions.
- The nonlinear phase trapping contributes to the flux enhancement of electrons above 20 keV.

Corresponding author: Shinji Saito, s.saito@nict.go.jp

Abstract

The temporal variation of the energetic electron flux distribution caused by whistler mode chorus waves through the cyclotron resonant interaction provides crucial information on how electrons are accelerated in the Earth's inner magnetosphere. This study employing a data-driven test-particle simulation demonstrates that the rapid deformation of energetic electron distribution observed by the Arase satellite is not simply explained by a quasi-linear diffusion mechanism, but is essentially caused by nonlinear scattering: the phase trapping and the phase dislocation. In response to upper-band whistler chorus bursts, multiple nonlinear interactions finally achieve an efficient flux enhancement of electrons on a time scale of the chorus burst. A quasi-linear diffusion model tends to underestimate the flux enhancement of energetic electrons as compared with a model based on the realistic dynamic frequency spectrum of whistler waves. It is concluded that the nonlinear phase trapping plays an important role in the rapid flux enhancement of energetic electrons observed by Arase.

Plain Language Summary

Energetic electrons could be a cause of satellite anomalies affected by electric discharge phenomena on its surface and interior materials. To minimize the anomalies through satellite operation, it is important to forecast the temporal variation of the energetic electron flux along the trajectories of a satellite. One of the causes of the variation of the electron flux is whistler mode waves, which are right-handed, circularly polarized electromagnetic waves that can resonate with energetic electrons. To understand how the electrons are accelerated in realistic situations, we have performed a data-driven numerical simulation to demonstrate electron scattering, by importing the observation data of the Arase satellite directly to the simulation. Results of the simulation reproduce the temporal variations of energetic electron flux distributions in burst of whistler mode waves. It is found that the nonlinear scattering contributes to the flux enhancement of energetic electrons. It is confirmed that a quasi-linear diffusion model, which has been used in general so far, cannot explain such a rapid flux enhancement. We conclude that the nonlinear scattering caused by the whistler burst plays an important role in the rapid flux enhancement of energetic electrons observed by the Arase satellite.

52 1 Introduction

53 Whistler mode chorus waves are bursty electromagnetic emissions that are often
 54 observed as the lower band mode below half of the electron cyclotron frequency f_{ce} and/or
 55 the upper band mode between $0.5f_{ce}$ and $1.0f_{ce}$. The Earth's magnetosphere naturally
 56 generates the whistler chorus with the injection of several tens of keV electrons associ-
 57 ated with substorms (e.g., Tsurutani & Smith, 1977; Miyoshi et al., 2003, 2013). The
 58 whistler chorus waves play an important role in accelerating energetic electrons over a
 59 wide energy range on the keV to MeV order through Doppler-shifted cyclotron resonance
 60 (Horne & Thorne, 2003). Cyclotron resonant interactions result in the pitch angle and
 61 energy diffusion of electrons bouncing along a magnetic field line, and more energetic elec-
 62 trons can resonate with chorus waves at higher magnetic latitudes. A quasi-linear the-
 63 ory, which assumes the resonant interactions by incoherent, broadband, and small-amplitude
 64 whistler waves, is commonly used to describe the evolution of the phase space density
 65 of radiation belt electrons. Numerical simulations based on the theory reproduce the evo-
 66 lution of electrons trapped in the Earth's magnetosphere on a time scale range from an
 67 hour to a day (Thorne et al., 2013; Glauert et al., 2014; Tu et al., 2014).

68 However, some previous observations suggest the rapid acceleration of energetic elec-
 69 trons on a time scale much shorter than the prediction based on a quasi-linear theory
 70 (Fennell et al., 2014; Kurita et al., 2018). This indicates that some efficient acceleration
 71 processes not described in this theory are involved. Many theoretical and simulation stud-
 72 ies have shown the importance of a nonlinear scattering process associated with the co-
 73 herent and bursty nature of the whistler chorus waves (e.g., Omura et al., 2007; Bort-
 74 nink et al., 2008; Lakhina et al., 2010; Saito et al., 2016). The contribution of the coher-
 75 ent nature of chorus waves, which is beyond the scope of the quasi-linear theory, plays
 76 an important role in the efficient acceleration of energetic electrons. In particular, rel-
 77 ativistic turning acceleration (RTA) (Omura et al., 2007) requires the coherent nature
 78 of whistler waves in order to efficiently accelerate electrons. Lakhina et al. (2010) also
 79 discussed the importance of the coherent and bursty nature of whistler chorus waves. They
 80 estimated the rate of the pitch angle change of electrons using coherent subelements with
 81 durations of tens of milliseconds or longer. For typical parameters of whistler chorus el-
 82 ements, their study showed that the coherent chorus elements can realize a more rapid
 83 pitch angle scattering of energetic electrons than a continuum of incoherent chorus waves
 84 as assumed in the quasi-linear theory. Previous studies have thus revealed that quasi-

85 linear models may underestimate electron scattering in terms of pitch angle and energy
86 by whistler chorus bursts.

87 As studied by Kurita et al. (2018), the Arase satellite (Miyoshi, Shinohara, et al.,
88 2018) observed the rapid flux enhancement of electrons with energies above 20 keV as-
89 sociated with an intense upper-band whistler chorus burst. They found that the evolu-
90 tion of electron pitch angle distributions in multi-energy channels occurs within 30 s. By
91 detailed data analysis of the cyclotron resonant condition between electrons and the cho-
92 rus burst, they concluded that the evolution is a consequence of wave-particle interac-
93 tions, which are faster than expected from a quasi-linear theory. Thus, it is of consid-
94 erable interest to examine numerically how the electrons are accelerated rapidly through
95 the wave-particle interactions on such a short time scale, using in situ observational data
96 obtained by Arase.

97 In this paper, we demonstrate electron scattering by an upper-band whistler cho-
98 rus burst with a duration of 32 s, using a test-particle simulation: Geospace Environ-
99 ment Modeling System for Integrated Studies - Radiation Belt with Wave-particle in-
100 teraction (GEMSIS-RBW) (Saito et al., 2012) with observational data obtained by the
101 Medium Energy Particle Experiment-electron analyzer (MEP-e; S. Kasahara et al. (2018))
102 and Onboard Frequency Analyzer (OFA; Matsuda et al. (2018)) in Plasma Wave Exper-
103 iment (PWE; Y. Kasahara et al. (2018)) onboard Arase. In Sec. 2, we describe the ob-
104 servational data set applied to the test-particle simulation. In Sec. 3, we describe the
105 simulation model and its initial conditions. In Sec. 4, we compare the temporal varia-
106 tions of electron flux distributions resulting from the simulation with the observational
107 data. Our test-particle simulation demonstrates that the upper-band whistler chorus burst
108 reproduces the Arase observations through the electron scattering by the nonlinear phase
109 trapping. In Sec. 5, we discuss the scattering processes in the whistler chorus burst, some
110 problems of our simulation, and potential future works. Finally, we conclude that the
111 nonlinear scattering, which should not be described by quasi-linear diffusion processes,
112 plays an important role in the deformation of electron flux distribution in a short du-
113 ration, as observed by Arase.

2 Arase observation

A rapid deformation of electron flux distribution at tens of keV during a period between 19:20:13 UT and 19:20:46 UT on 8 April 2017 was reported by Kurita et al. (2018). Arase was located near the magnetic equator (magnetic latitude of $0.2^\circ - 1.5^\circ$), at the magnetic local time of 4.3 – 4.5 h, and the radial distance of 5.5 Earth radii, corresponding to the McIlwain L (L_m) of about 5.4. Magnetic field data obtained by the Magnetic Field Experiment (MGF; Matsuoka, Teramoto, Nomura, et al. (2018)) onboard Arase show a background magnetic field intensity of 170 nT, indicating the local electron cyclotron frequency f_{ce} of 4.7 kHz. The plasma density $N = 3.4 \text{ cm}^{-3}$ was estimated by Kurita et al. (2018) on the basis of HFA and MGF measurements, where HFA is the high-frequency analyzer onboard Arase (Kumamoto et al., 2018), indicating the local electron plasma frequency f_{pe} of 16.5 kHz and thereby the frequency ratio f_{pe}/f_{ce} of about 3.5.

Figure 1 is the summary plot of the event. The OFA magnetic spectrum (top panel) shows an intense upper-band whistler chorus burst at frequencies over $0.5f_{ce}$. The wave amplitude is highly variable in time and frequency. The maximum instantaneous amplitude of the magnetic fluctuation exceeds 100 pT. Kurita et al. (2018) estimated the wave normal angle of the upper-band whistlers by the singular value decomposition method (Santolík et al., 2003). They found that the burst propagates in the quasi-parallel direction of the background magnetic field. Bottom panels of Figure 1 show electron flux distributions obtained by MEP-e at four time intervals. Over 32 s represented by the panels, the flux of >20 keV increases at pitch angles of 70 – 80 degrees, while the flux of <20 keV decreases at pitch angles of 40 – 50 degrees. Because the flux variation seems to occur on the resonant ellipses of the upper-band whistlers, Kurita et al. (2018) concluded that the low-energy electrons are accelerated to higher energies through the cyclotron resonance with the upper-band whistler chorus burst.

3 Simulation models and initial conditions

We perform a test-particle simulation that demonstrates the electron scattering by the upper-band whistler chorus burst on a magnetic field line. The upper-band whistlers are assumed to be generated at the magnetic equator and propagate away from the equator along the field line. We set wave amplitudes and frequencies on the basis of the OFA

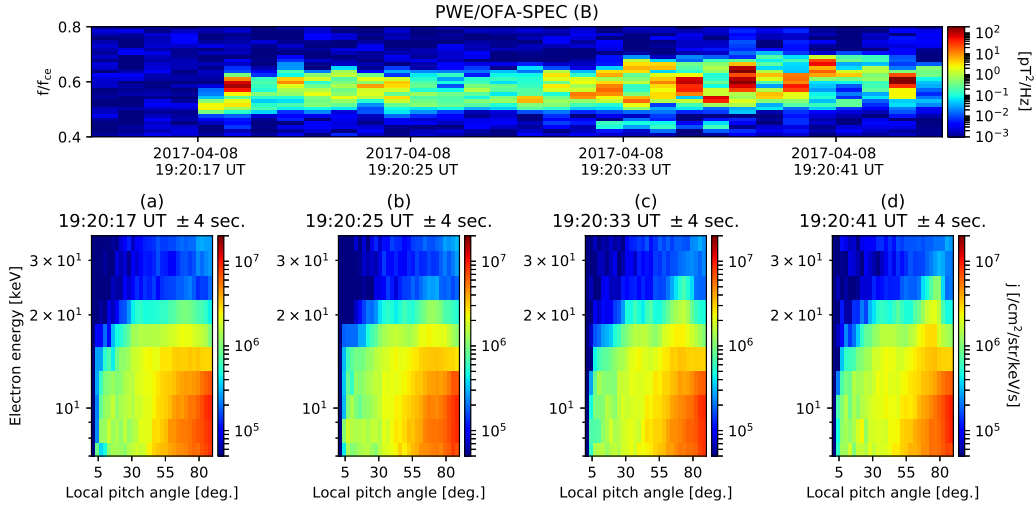


Figure 1. Observation by Arase located at the magnetic latitude of $0.2^\circ - 1.5^\circ$, the magnetic local time of 4.3 – 4.5 h, and the radial distance of 5.5 Earth radii ($L_m \sim 5.4$). (Top) Dynamic frequency spectrum of magnetic fluctuations obtained from PWE/OFA. (Bottom) Electron flux distributions as functions of pitch angle and energy obtained from MEP-e at time intervals at around 19:20:17, 19:20:25, 19:20:33, and 19:20:41 UT. Electrons responsible for each flux distribution are detected in the time range of ± 4 s.

145 magnetic field spectrum shown in Fig. 1. The simulation solves the equations for adi-
 146 abatic and non-adiabatic momentum change of 10^6 electrons by the upper-band whistlers.
 147 We set particle weights for all the electrons on the basis of the electron flux distribution
 148 obtained by MEP-e before the upper-band whistlers are enhanced. By using the weights
 149 for the electrons, we can calculate the time variation of the electron flux distribution at
 150 any place along the field line throughout the simulation. The following subsections de-
 151 scribe the details of the test-particle model, the wave model, and the initial condition
 152 used in the simulation.

153 3.1 Test-particle model

154 We use the test-particle simulation code GEMSIS-RBW (RBW) (Saito et al., 2012)
 155 to demonstrate the temporal variation of energetic electron flux distribution. Using the
 156 RBW simulation model, we calculate the adiabatic motion of electrons along a field line

157 using the equations of magnetic mirror motion of the guiding center,

$$158 \quad \frac{dp_{\parallel}}{dt} = -\frac{\mu}{\gamma} \frac{\partial B}{\partial s}, \quad (1)$$

$$159 \quad \frac{ds}{dt} = \frac{p_{\parallel}}{m_o \gamma}, \quad (2)$$

161 where $\mu = p_{\perp}^2 / (2m_o B)$ is the first adiabatic invariant. The invariant is assumed to be
 162 constant as the mirror force is solved with the equation. Here, the relativistic Lorentz
 163 gamma γ is $\sqrt{1 + p^2 / (m_o c)^2}$, B is the magnetic field intensity at the electron position
 164 s , $p^2 = p_{\parallel}^2 + p_{\perp}^2$, p_{\parallel} and p_{\perp} are electron momenta parallel and perpendicular to the mag-
 165 netic field, respectively, m_o is electron rest mass, and c is the light speed. The equations
 166 are solved by using the 4th-order Runge–Kutta method. In addition to the adiabatic mir-
 167 ror motion, the RBW simulation demonstrates the propagation of wave packets along
 168 the field line with its own group velocity. The group velocity based on the cold plasma
 169 dispersion relation is calculated at packet positions. Each wave packet has a wave am-
 170 plitude and frequency, which are constant over time.

171 By calculating multiple packets traveling along the field line in the RBW model,
 172 we can estimate the wave frequency and amplitude acting on each of the electrons on
 173 the field line. The wavenumber at the electron position k_s is calculated from the linear
 174 dispersion relation of whistler waves with the the frequency f_s , and then right circularly
 175 polarized electromagnetic fluctuations $\delta\mathbf{E}$ and $\delta\mathbf{B}$ at the electron position are constructed
 176 using the RBW model. The temporal variation of the magnetic wave phase ϕ at the elec-
 177 tron position is

$$178 \quad \phi = 2\pi f_s t - k_s v_{\parallel} t + \phi_o. \quad (3)$$

179 Here, ϕ_o is the wave phase at which the wave-particle interaction starts. Note that ϕ is
 180 assigned to each of the electrons, which is the important core method for the RBW model.
 181 By using the electromagnetic fluctuations, we can solve the following equation of mo-
 182 tion using the RBW model,

$$183 \quad \frac{d\mathbf{p}}{dt} = q_e (\delta\mathbf{E} + \mathbf{v} \times (\mathbf{B} + \delta\mathbf{B})), \quad (4)$$

184 where \mathbf{v} is the vector of electron velocity. Wave data applied to Eq. (4) are updated ev-
 185 ery Δt (~ 0.035 ms) which is the time resolution of the solver of the guiding-center equa-
 186 tions (Eqs. (1) and (2)), whereas the time resolution for the equation of motion (Eq. 4)
 187 is $\delta t = \tau_{gyro}/64$, which is quite shorter than Δt , where τ_{gyro} is the in situ electron gy-
 188 ration period. The equation of motion is solved by the Buneman–Boris method (Buneman,

189 1993). The equation of motion is used to calculate $\Delta\mathbf{p}$, which is the change in \mathbf{p} in Δt ;
 190 then $\Delta\mathbf{p}$ is reflected in the guiding-center equations (Eqs. (1) and (2)). Then, the first
 191 adiabatic invariant μ is updated using the magnetic field intensity at the electron po-
 192 sition, corresponding to the break of μ caused by the electron scattering. By using the
 193 above sequence of calculations, we can solve the equations of magnetic mirror motion
 194 coupled with the equation of motion in electromagnetic fluctuations of whistler mode
 195 waves propagating along the field line. The RBW model has been successfully applied
 196 to various wave-particle interaction phenomena in radiation belts, pulsating auroras, and
 197 microbursts (Saito et al., 2012, 2016; Miyoshi, Oyama, et al., 2015; Miyoshi, Saito, et
 198 al., 2015; Miyoshi et al., 2020).

199 3.2 Wave model

200 Wave packets are released every 1 ms from the magnetic equator according to the
 201 OFA magnetic spectrum shown in Fig. 1. The OFA resolves 15 frequencies between $0.5f_{ce}$
 202 and $0.7f_{ce}$. The frequency of each wave mode is defined as the discrete frequency f^i ,

$$203 f^i = f_o + \Delta f \times i, \quad (5)$$

204 where f_o is 2.368 kHz, Δf is 64 Hz, and i is an integer between 1 and 15. Since the time
 205 resolution of the OFA is 1 s, the amplitude of wave packets released every Δt varies ev-
 206 ery second. When there are multiple modes at the electron position, the RBW model
 207 is used to construct electromagnetic fluctuations acting on the electron by linearly su-
 208 perimposing these modes. On the basis of statistical studies of the upper band chorus
 209 distribution (e.g., Bortnik et al., 2007), we assume that wave packet propagation is lim-
 210 ited to a magnetic latitude of 10 degrees. Note that there is no correlation of wave phase
 211 among wave modes in the simulation. Moreover, we assume that the phase difference be-
 212 tween the wave phase and the electron gyrophase is randomly set between 0 and 2π when
 213 the electron passes through the magnetic latitudes of 10 degrees from higher latitudes.

214 3.3 Initial conditions

215 The magnetic field intensity along the field line in this simulation is assumed to be
 216 equal to the Earth's dipole field. On the basis of the MGF data of Arase, which was lo-
 217 cated close to the magnetic equator, the equatorial magnetic field intensity B_{eq} is esti-
 218 mated to be 170 nT. The background magnetic field is assumed to be the dipole field;

219 thus, the magnetic field strength along the field line is

$$220 \quad B(\lambda) = 170 \times 10^{-9} \frac{\sqrt{1 + 3 \sin^2 \lambda}}{\cos^6 \lambda}, \quad (6)$$

221 where λ is latitude. On the basis of the HFA and MGF measurements, as described in
 222 Sec. 2, the estimated plasma density $N = 3.4 \text{ cm}^{-3}$ is applied in this simulation. Here,
 223 as in the previous simulation (Miyoshi, Oyama, et al., 2015), we assume that the plasma
 224 density is constant along the field line up to the magnetic latitude of 10 degrees.

225 The number of electrons in the present simulation is 10^6 . These are distributed along
 226 the magnetic field line with random bounce phases. Their equatorial pitch angles range
 227 from the loss cone angle to slightly less than 90 degrees, and the kinetic energy ranges
 228 from 5 to 40 keV. The weight of electrons at energy E and the equatorial pitch angle α_{eq}
 229 are derived from the weight table W ,

$$230 \quad W(E, \alpha_{eq}) = \frac{j(E, \alpha_{eq})}{j_u(E, \alpha_{eq})}. \quad (7)$$

231 Here, $j(E, \alpha_{eq})$ is the flux distribution to be reproduced, and $j_u(E, \alpha_{eq})$ is the flux dis-
 232 tribution calculated from the electrons with the unit weight. $j(E, \alpha_{eq})$ can be reproduced
 233 by setting the weight of the electrons. The weight of electrons is determined to fit the
 234 distribution function obtained by MEP-e just before the chorus burst appears. The weight
 235 is constant over time and there is no additional injection of electrons throughout the sim-
 236 ulation. The simulation starts from 2017-04-08 19:20:13 UT at which wave packets start
 237 to inject from the equator following the OFA shown in Figure 1. The simulation time
 238 t is the time that elapsed from the start.

239 4 Simulation results

240 Figure 2 shows electron flux distributions calculated at the equator in the simu-
 241 lation. The time intervals labeled on the panels (a – d) correspond to the time intervals
 242 of observations for the flux distributions shown in the lower panels in Figure 1. The tem-
 243 poral evolution of electron fluxes shows that the electron flux increases at energies higher
 244 than 20 keV within 32 s. At energies lower than 20 keV, the electron flux at the pitch
 245 angles of 40 – 50 degrees decreases. These characteristics of flux deformation are sim-
 246 ilar to those of MEP-e shown in Figure 1.

247 To compare these distributions more directly, we plot the pitch angle distributions
 248 at 14.3, 17.1, 20.5, and 24.5 keV of the Arase observations (blue lines) with those of the

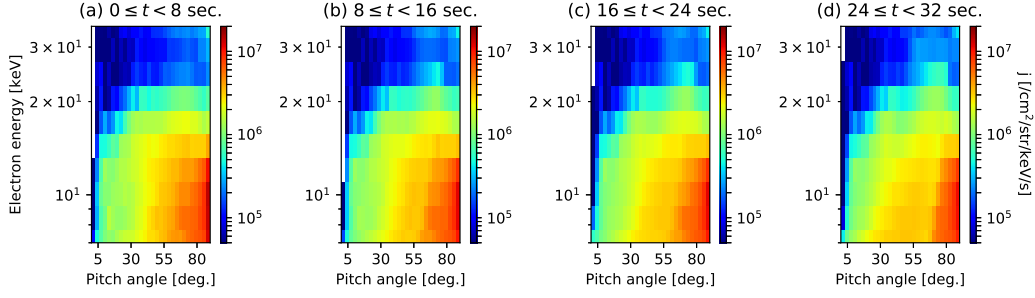


Figure 2. Equatorial electron flux distributions calculated from RBW simulation as a function of pitch angle and energy. The flux distributions are calculated during (a) $0 \leq t < 8$ s, (b) $8 \leq t < 16$ s, (c) $16 \leq t < 24$ s, and (d) $24 \leq t < 32$ s. These time ranges correspond to 19:20:17 UT \pm 4 s, 19:20:25 UT \pm 4 s, 19:20:33 UT \pm 4 s, and 19:20:41 UT \pm 4 s, respectively.

249 simulation (red lines) in Figure 3. The Arase observations over 8 s are averaged, whereas
 250 black error bars show the standard deviations of the Arase observations at each pitch
 251 angle and energy bins during the indicated time interval. In both the simulation and ob-
 252 servation, electron fluxes at around the pitch angle of 50 degrees decrease over time at
 253 energies of 14.3 and 17.1 keV, whereas those at around the pitch angle of 75 degrees at
 254 energies of 20.5 and 24.5 keV increase. A butterfly distribution is formed at energies higher
 255 than 20 keV. It is shown that the simulation reproduces the characteristics of the ob-
 256 served flux enhancement.

257 Figure 4 shows the initial flux distributions of electrons that contribute to the fluxes
 258 within the energy range between 23.5 and 25.5 keV and the pitch angle range between
 259 70 and 80 degrees in (a) $0 \leq t < 8$, (b) $8 \leq t < 16$, (c) $16 \leq t < 24$, and (d) $24 \leq$
 260 $t < 32$ s. Here, we define the pitch angle and energy ranges as Λ . As shown in panel
 261 (a), the initial flux distribution of electrons has a peak in the Λ at the time of less than
 262 8 s. Only a small fraction of the electrons originate from outside of Λ at this moment.
 263 At later times, as shown in panels (b-d), the distribution spreads in both directions of
 264 energy and pitch angle, and the peak of the flux distribution moves toward lower ener-
 265 gies and smaller pitch angles. At the time interval shown in panel (d), there is a peak
 266 of the distribution at the pitch angle between 40 and 50 degrees and the energy between
 267 15 and 16 keV, indicating that the electrons that were initially distributed there dom-
 268 inate Λ .

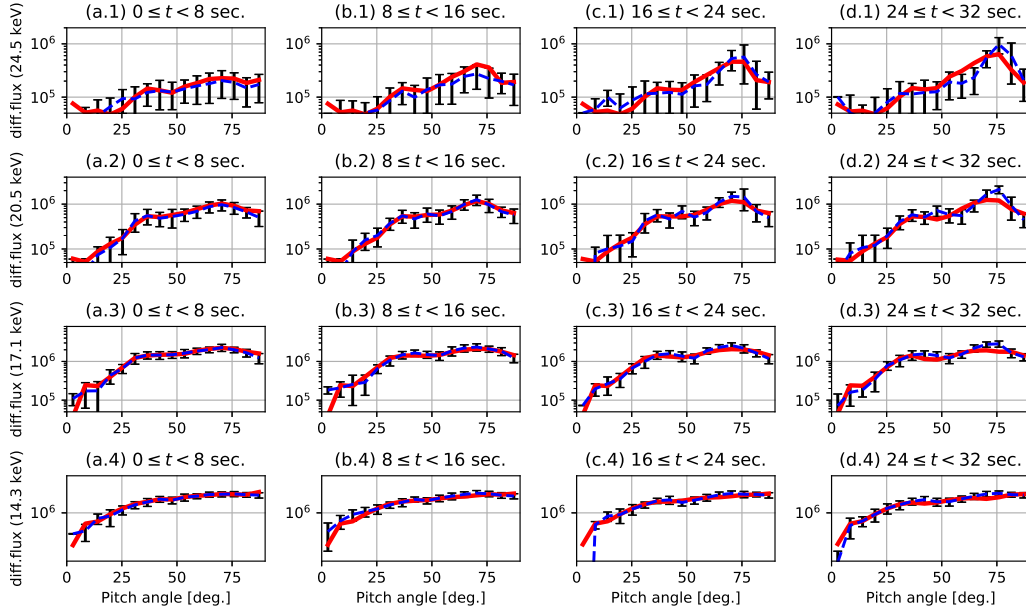


Figure 3. Pitch angle distributions at 14.3, 17.1, 20.5, and 24.5 keV. Blue lines are electron fluxes taken from the MEP-e onboard Arase averaged over 8 s, black error bars are the standard deviations of the fluxes obtained during the time interval, and red lines are calculated from the RBW simulation.

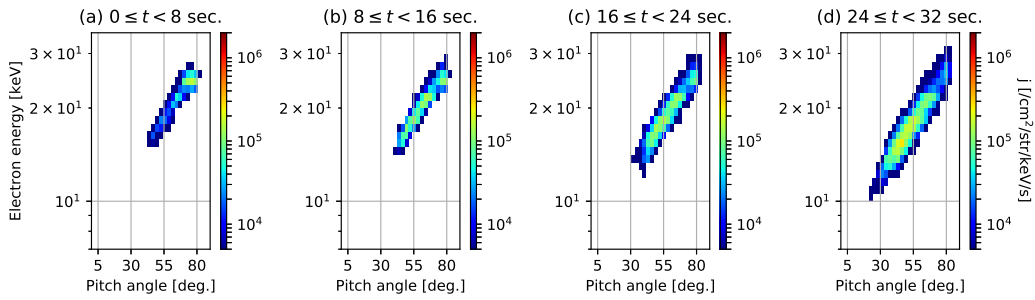


Figure 4. Initial flux distributions of electrons contributing to flux within the energy range between 23.5 keV and 25.5 keV and the pitch angle range between 70 and 80 degrees in the time ranges of (a) $0 \leq t < 8$, (b) $8 \leq t < 16$, (c) $16 \leq t < 24$, and (d) $24 \leq t < 32$ s.

269 Figure 5 confirms whether the pitch angle change can be realized with a quasi-linear
 270 diffusion model. The black-dashed line in the top panel shows the magnetic wave power
 271 in frequency averaged in time during the burst event, calculated from the OFA magnetic
 272 spectrum. The dashed red line is a Gaussian fitting curve for the time-averaged frequency
 273 spectrum. The Gaussian fitting gives the maximum amplitude of 33.6 pT, the center of
 274 frequency of $0.59f_{ce}$, and the frequency band width of $0.027f_{ce}$. With the derived pa-
 275 rameters of the magnetic wave power distribution, we calculate the pitch angle diffusion
 276 coefficients of the quasi-linear diffusion model (Albert, 1999) at energies of 10, 20, and
 277 30 keV. Here, the coefficients are averaged in the bounce motion. As electrons move along
 278 the distribution shown in Figure 4(d) before reaching Λ , the averaged pitch angle coef-
 279 ficient of the electrons would be less than 2×10^{-3} [/sec.]. We found in Figure 4 (d) that
 280 the main flux source contributing to the formation of the butterfly distribution is at a
 281 pitch angle between 40 and 50 degrees and an energy between 15 and 16 keV. From a
 282 simple estimation, a value corresponding to a pitch angle diffusion coefficient is about
 283 4×10^{-3} [/sec.] as electrons at the source region ($\alpha_{eq} = 45$ degrees) move to the flux
 284 peak at 24.5 keV ($\alpha_{eq} = 75$ degrees) within 32 s. This value seems to be slightly larger
 285 than the diffusion coefficients estimated using the quasi-linear diffusion model, but roughly
 286 of the same order. It suggests that some electrons initially at 15 keV can contribute to
 287 the butterfly distribution formation through pitch angle scattering with comparable timescales
 288 predicted by the quasi-linear process.

289 Figure 6 shows the probability of nonlinear scattering of electrons with energies be-
 290 tween 24 and 25 keV at $t = 32$ s as a function of equatorial pitch angle. The probab-
 291 ility is defined as N_{rapid}/N_{total} with the energy range in a pitch angle bin, where N_{rapid}
 292 is the number of electrons that have experienced a rapid change in the pitch angle and
 293 the energy at least once during 32 s and N_{total} is the total number of electrons. Here,
 294 the number of electrons in each bin is calculated considering particle weights defined by
 295 the initial flux distribution. The rapid change for an electron means that a value of $D_{TP} =$
 296 $\Delta\alpha_{eq}^2/(2\Delta t)$ corresponding to an instantaneous pitch angle diffusion coefficient exceeds
 297 the threshold coefficients $D_{th} = 0.05, 0.1, \text{ and } 0.2$, where $\Delta\alpha_{eq}$ is an equatorial pitch
 298 angle change calculated every $\Delta t = 0.2$ s. The threshold coefficients are 20 - 100 times
 299 larger than the pitch angle coefficients in Figure 5. As seen in Figure 6, there is a peak
 300 in pitch angles of 70 and 80 degrees at each D_{th} . Around a pitch angle of 75 degrees, al-
 301 most all electrons experience $D_{TP} > 0.05$ at least once during the burst. The value is

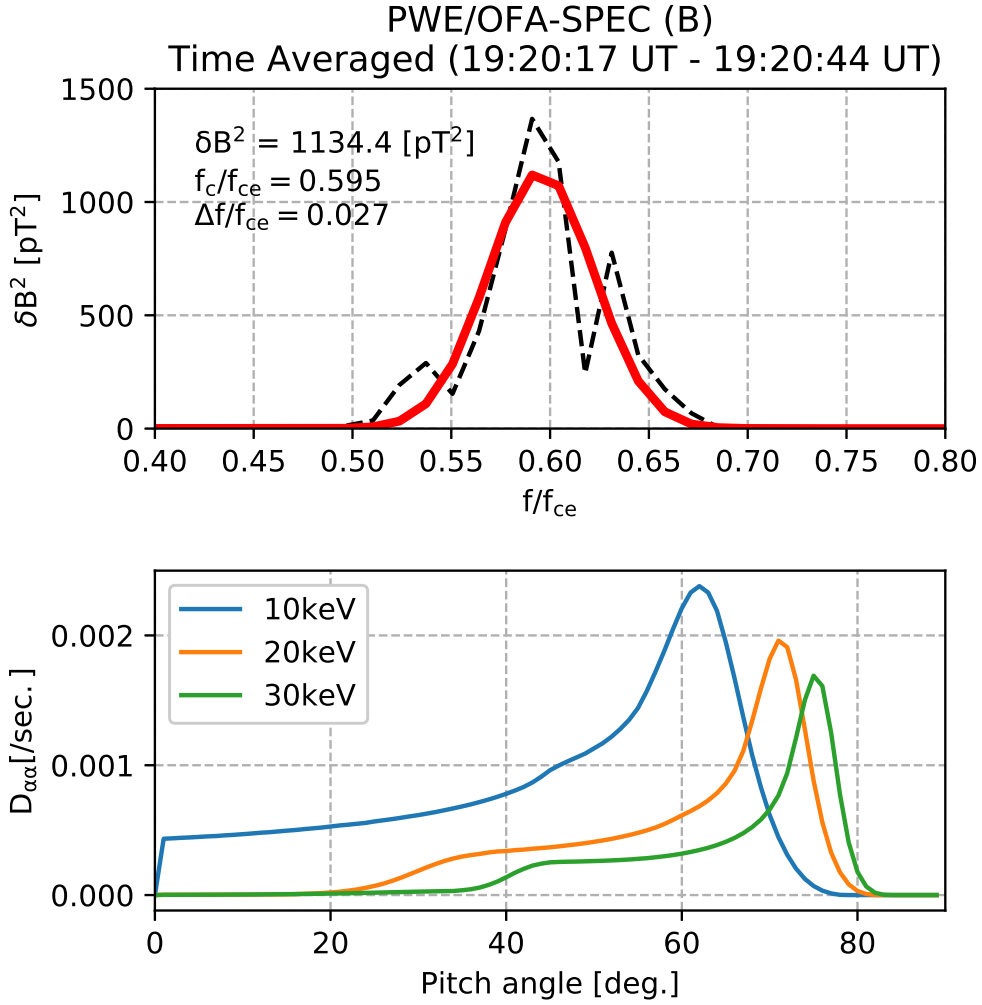


Figure 5. (Top) Magnetic frequency spectrum averaged in time during the burst event obtained from PWE/OFA (Black-dashed) and a Gaussian fitting curve for the time-averaged frequency spectrum (Red). (Bottom) Bounce-averaged, pitch angle diffusion coefficients as a function of pitch angle with energies of 10, 20, and 30 keV. The quasi-linear model uses the Gaussian distribution of magnetic wave power as shown in the top panel, which has the maximum amplitude of 33.6 pT, the center of frequency of $0.59 f_{ce}$, and the frequency band width of $0.027 f_{ce}$. We assume a Gaussian distribution of the wave propagation angle with the half width of 45 degrees, centered at the zero degree along the magnetic field line.

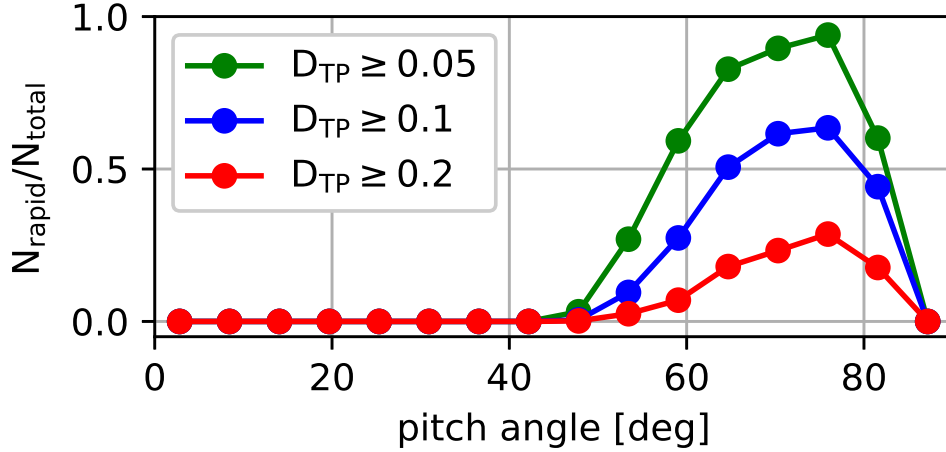


Figure 6. Probability of nonlinear scattering for electrons with energies between 24 and 25 keV at $t = 32$ s as a function of equatorial pitch angle.

302 about 20 times larger than the diffusion coefficients. About 30% of electrons at the peak
 303 experience a rapid scattering with $D_{TP} > 0.2$, which is 100 times larger than the es-
 304 timation with the quasi-linear model. The peaks of $N_{\text{rapid}}/N_{\text{total}}$ in pitch angle are within
 305 a range of electron flux enhancement shown in the top panels ($E = 24.5$ keV) in Figure
 306 3. From the OFA spectrum (Figure 1), the maximum instantaneous amplitude is esti-
 307 mated to be about 120 pT, which is four times higher than the average amplitude. If we
 308 assume a 16 ($= 4^2$) times higher magnetic power distribution, pitch angle diffusion co-
 309 efficients would be estimated to be up to 0.032 [1/sec.]. The diffusion coefficients estimated
 310 using the quasi-linear model cannot exceed 0.05.

311 We examine linear/nonlinear scattering processes in more detail by analyzing the
 312 motion of typical electrons in the simulation. Figure 7 shows the time histories of en-
 313 ergy and equatorial pitch angle of five electrons labeled as A to E, which are sampled
 314 from 100 electrons with energies between 15 and 16 keV and equatorial pitch angles be-
 315 tween 40 and 50 degrees at $t=0$. Because the whistlers propagate away from the equa-
 316 tor up to the magnetic latitude of 10 degrees, electrons have opportunities to be scat-
 317 tered through cyclotron resonance when they travel toward the equator at magnetic lat-
 318 itudes less than 10 degrees. Thus, electrons can be scattered every half of the bounce
 319 period (~ 0.5 s), as seen in all the time histories. Almost all scattering times are on the
 320 order of 100 ms or shorter. In many cases, electrons experience energy changes of less

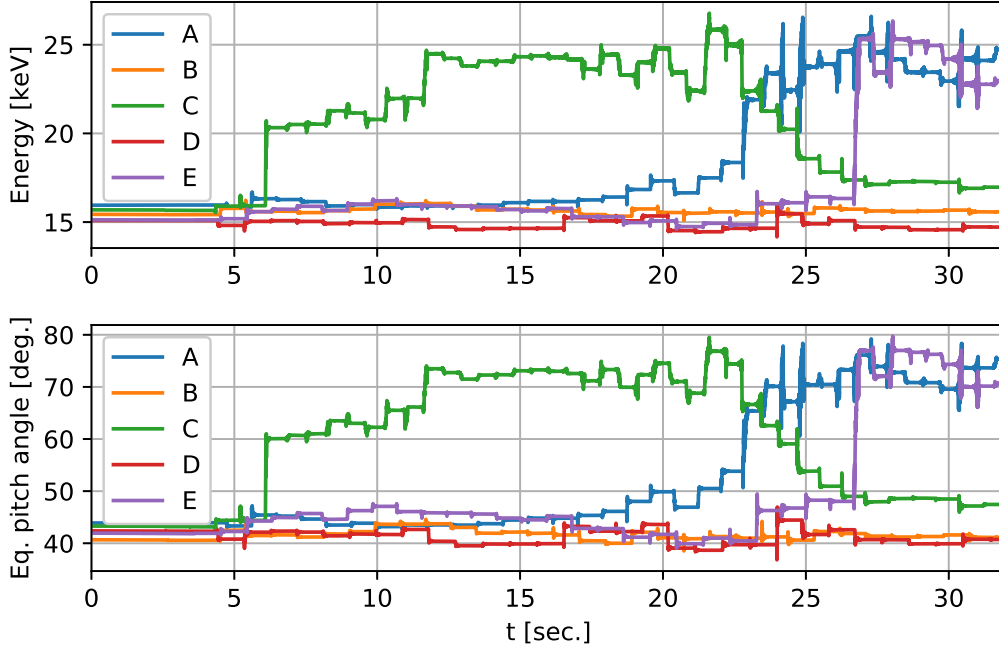


Figure 7. Time histories of the energy (top) and equatorial pitch angle (bottom) of five electrons labeled as A to E. The initial pitch angle and energy are between 40 and 50 degrees and between 15 and 16 keV, respectively.

321 than 1 keV, but in some cases, the interaction increases or decreases their energy higher
 322 than 1 keV at a single scattering.

323 Figure 8 shows the results of a detailed analysis of electron E. The top panel shows
 324 the energy time history of electron E, which is the same as that shown as the purple line
 325 in Figure 7. For the simulation time of less than 26 s, the electron undergoes energy changes
 326 of 1 keV or less in each of the scattering events. We label one of the events as (I). In the
 327 time range between 26 and 27 s, the electron gains an energy of about 8 keV, which is
 328 labeled as (II). Soon after the efficient energy gain, the electron loses an energy of about
 329 2 keV, which is labeled as (III). For the three events labeled here, we show the distance
 330 of the electron from the magnetic equator (2nd row), the kinetic energy (3rd row), the
 331 inhomogeneity ratio S (4th row), and the phase differences ζ between the wave phase
 332 and the electron gyrophase (5th row). As described by Omura et al. (2007), the inho-
 333 mogeneity ratio is

$$334 \quad S = \frac{1}{2kv_{\perp}\Omega_w\delta^2} \left[\left(2 + \delta^2 \frac{\Omega_e - \gamma\omega}{\Omega_e - \omega} \right) V_R - \frac{k\gamma v_{\perp}^2}{\Omega_e} \right] \frac{\partial\Omega_e}{\partial s}, \quad (8)$$

335 where $\delta^2 = 1 - (\omega/ck)^2$, $\Omega_w = -q_e\delta B/m_o$, $V_R = (\omega - \Omega_e/\gamma)/k$, v_\perp is the speed of an
 336 electron in the direction perpendicular to the background magnetic field, and Ω_e is the
 337 angular electron cyclotron frequency. The inhomogeneity ratio and the phase difference
 338 are calculated for 15 wave modes described in Sec. 3.2.

339 To estimate the energy change and the interaction time of each of the events, we
 340 calculate the fitting curve using the function based on the hyperbolic tangent curve,

$$341 \quad F(t) = \frac{\Delta E}{2} \left(1 + \tanh \frac{t - t_c}{t_w} \right) + E_o, \quad (9)$$

342 by solving a nonlinear least-squares problem by an algorithm (Branch et al., 1999) that
 343 is used in the function `scipy.optimize.curve_fit()` in SciPy library (Virtanen et al.,
 344 2020). Here, ΔE is the amount of energy change, t_c is the center time of the scattering
 345 event, t_w is the half width of the time interval of the energy change, and E_o is the ini-
 346 tial value of the function. The curve obtained using the estimated parameters is shown
 347 as the blue dashed lines in the third row in Figure 8, and the parameters are shown in
 348 each of the panels. Event (I) has the smallest energy change ($\Delta E = 130$ eV) with the
 349 shortest duration of 4.8 ms ($= 2t_w$) among the three events. On the other hand, event
 350 (II) has the longest duration of 100.4 ms with the largest energy change (7.98 keV). Event
 351 (III) shows the energy reduction (-1.93 keV) with a moderate duration of 27.4 ms. Note
 352 that the pitch angle immediately before the rapid energy loss is relatively large ($\alpha_{eq} >$
 353 75 degrees), as is shown in Figure 7.

354 We calculate the inhomogeneity ratio S (Omura et al., 2007) for 15 wave modes,
 355 which is the key parameter for the resonant phase trapping of electrons. The necessary
 356 condition for the trapping is $|S| \leq 1$, which satisfies the pendulum equation for the phase
 357 difference ζ . When the pendulum equation is satisfied, the electrons are trapped in the
 358 wave phase and then gain energy efficiently. Bortnik et al. (2008) defined the inhom-
 359 ogeneity forcing term ρ , which is used to categorize three scattering types: the linear scat-
 360 tering, the phase trapping, and the phase dislocation. The condition of $\rho < 1$ leads to
 361 the diffusive behavior of electrons, whereas the condition of $\rho \gg 1$ leads to the phase
 362 dislocation, which generally reduces the electron energy. When $\rho \sim 1$, some electrons
 363 are trapped by a wave, leading to the efficient energy gain of electrons. Saito et al. (2016)
 364 showed that $S^2\rho^2 = 1$, so the three types of scattering are also categorized on the ba-
 365 sis of S , namely, $|S| \gg 1$ for linear scattering, $|S| \sim 1$ or slightly less for the phase
 366 trapping, and $|S| \ll 1$ for the phase dislocation. The inhomogeneity ratio for 15 wave

367 modes in event (I) shows that all $|S|$ values are much larger than 1 within the duration
 368 of the small energy change, indicating the linear scattering. The time histories of ζ for
 369 15 wave modes do not show any signature of the phase trapping. Several high-frequency
 370 modes have ζ decreasing monotonically, whereas others have convex profiles indicating
 371 that the resonance conditions $d\zeta/dt \sim 0$ are satisfied at the peak of ζ . In event (II),
 372 several wave modes have $|S| \sim 1$ or slightly less during the efficient energy gain. The
 373 phase differences ζ of several modes remain roughly constant. It means that the elec-
 374 tron is phase-trapped by some of these modes. Thus, the electron undergoes efficient en-
 375 ergy gain over a duration longer than that of event (I). In the case of event (III), sev-
 376 eral wave modes have S values close to zero, and the electron loses energy, whereas $d\zeta/dt$
 377 of the wave modes is close to zero. The signature of event (III) is consistent with that
 378 of the phase dislocation.

379 We calculate the energy time histories of 100 electrons that have had the initial en-
 380 ergy between 15 and 16 keV and the initial equatorial pitch angle between 40 and 50 de-
 381 grees. From the entire dataset of the time histories, we estimate t_c and ΔE in each of
 382 the scattering events by using the fitting method as used in Figure 8. In each of the scat-
 383 tering events, we calculate the inhomogeneity ratio for 15 wave modes at t_c . A total of
 384 3,413 scattering events are identified from the dataset. Here, we choose scattering events
 385 whose standard deviation of ΔE is smaller than the estimated ΔE . The qualified event
 386 list is further grouped into two classes: weak and intense, according to the magnitude
 387 of ΔE , which are defined as $10\text{eV} \leq |\Delta E| < 100\text{eV}$ and $1\text{keV} \leq |\Delta E| < 10\text{keV}$, re-
 388 spectively. We further classify each of the two classes of the events into two types ac-
 389 cording to the sign of ΔE , that is, positive and negative.

390 Figure 9 shows the probability density functions (PDFs) of the inhomogeneity ra-
 391 tio S calculated at t_c for the two types in two classes. Note that the integral of the PDFs
 392 over S becomes unity. The number of identified events for each of the four cases is shown
 393 as N . The PDFs for intense events (left panels) show a clear peak at $|S|$ slightly lower
 394 than 1. According to the classification of the scattering processes discussed by Bortnik
 395 et al. (2008), the intense events are expected to be accompanied by phase trapping or
 396 phase dislocation. Considering the characteristics of the scattering processes, it is shown
 397 that the phase trapping and phase dislocation contribute to the intense-positive and intense-
 398 negative events, respectively. Note that the PDFs of the intense-negative events show
 399 the distribution confined slightly closer to $|S| = 0$ than that of the intense-positive events.

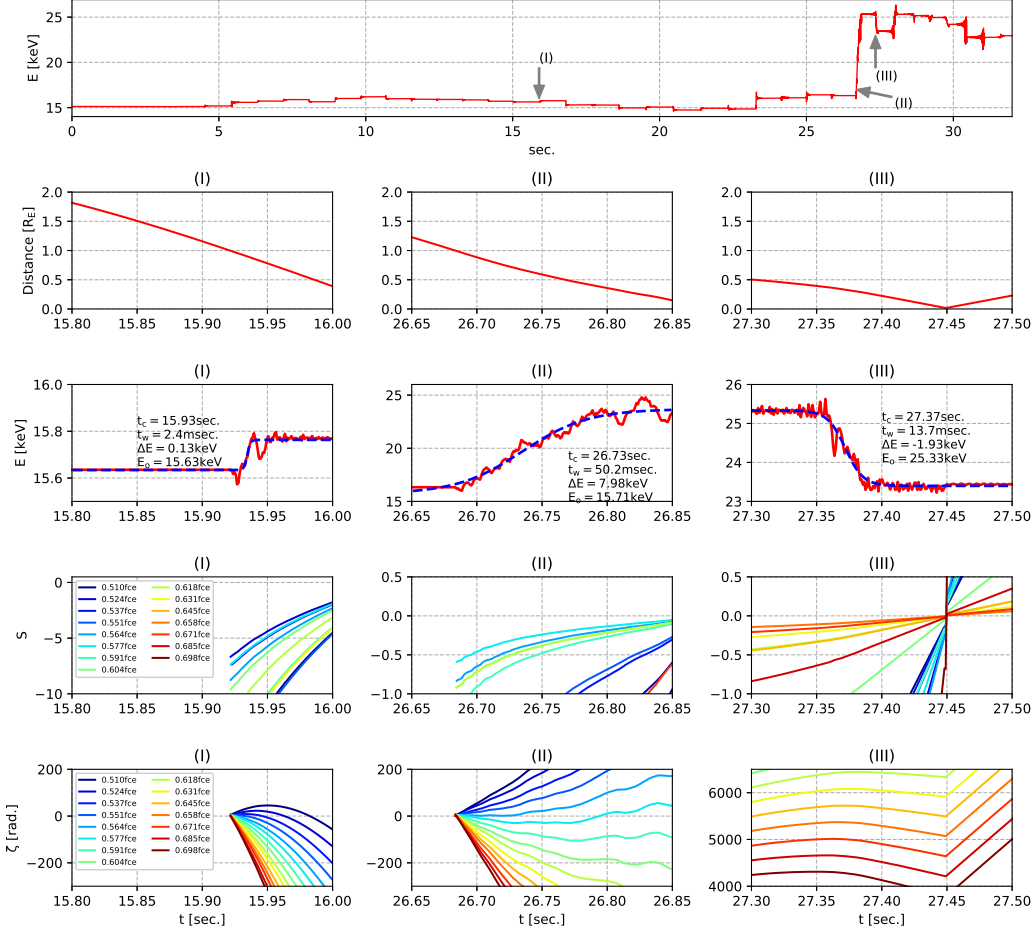


Figure 8. Results of a detailed analysis of electron E. (Top panel) Time history of the electron energy. (2nd row) Distance from magnetic equator in events (I), (II), and (III) labeled in top panel. (3rd row) The red line shows an enlarged view of the time history of the electron energy in each of the events. The blue dashed line is the curve fitting of the red line through the hyperbolic tangent function. The fitting parameters are shown in each of the panels. (4th row) Inhomogeneity ratio of the electron E associated with 15 wave modes. (Bottom row) Phase differences between the electron gyrophase and the wave phases of 15 wave modes.

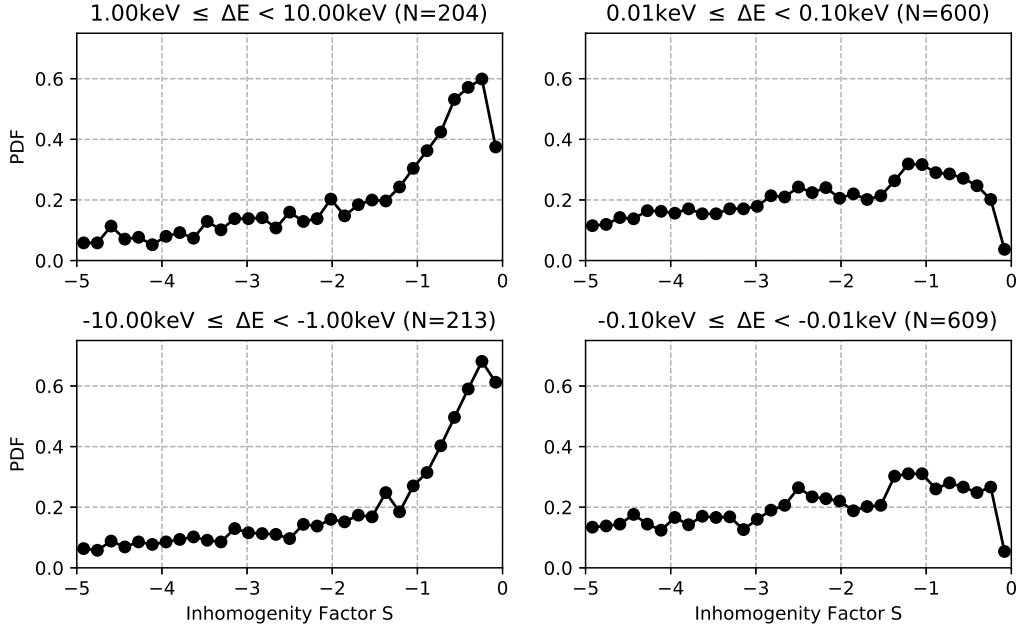


Figure 9. Probability distribution functions of the inhomogeneity ratio S for (upper left) intense-positive, (lower left) intense-negative, (upper right) weak-positive, and (lower right) weak-negative scattering events. The scattering events are identified from the energy–time histories of 100 electrons by the fitting method of the hyperbolic tangent fitting function for estimating t_c and ΔE . The inhomogeneity ratios for 15 wave modes for each of the electrons are calculated at t_c .

400 The slight difference in the distributions may reflect the differences in the conditions be-
 401 tween the phase dislocation and the phase trapping. In weak events, there is no signif-
 402 icant peak on the PDFs. Moreover, unlike the intense events, the PDFs tend to become
 403 smaller with decreasing $|S|$ when $|S| < 1$. On the other hand, at $|S| > 1$, the PDFs
 404 tend to be higher and relatively flatter than those in intense events. It is indicated that
 405 the linear scattering, which has $|S| \gg 1$, dominates both the weak-positive and weak-
 406 negative events.

407 Table 1 shows the probabilities calculated from the integral of PDFs in $|S| < 1$
 408 for the four categorized events. The integral of the PDF for the intense-positive events
 409 shows that roughly half of the wave modes at t_c have $|S| < 1$. The intense-negative events
 410 also show the high probabilities of wave modes with $|S| < 1$. It is clear that the wave
 411 modes that lead to nonlinear scatterings definitely contribute to the intense events. On

Table 1. Integral of PDFs in $|S| < 1$ for each of the scattering events.

	Intense	Weak
Positive	46.1 %	21.4 %
Negative	49.9 %	22.1 %

412 the other hand, in weak events, about 80% of the wave modes are found to be beyond
 413 the range ($|S| > 1$), indicating the dominance of the linear scattering.

414 5 Discussion

415 Our simulation results reproduce the temporal variation of the electron flux dis-
 416 tribution observed by Arase (Figures 1-3). A pitch angle distribution at 24.5 keV pro-
 417 duces a butterfly distribution within 32 s because of an upper-band chorus burst. It has
 418 a flux peak of the pitch angle between 70 and 80 degrees. The main flux source contribut-
 419 ing to the formation of the butterfly distribution is at a pitch angle between 40 and 50
 420 degrees and an energy between 15 and 16 keV at $t=0$ (Figure 4). From a simple estima-
 421 tion, we confirmed that some electrons initially at 15.5 keV may possibly contribute to
 422 the formation of the butterfly distribution through a quasi-linear process (Figure 5). How-
 423 ever, we found that the instantaneous pitch angle changes (D_{TP}) of some electrons are
 424 much larger than those in the quasi-linear process. Electrons that experience $D_{TP} \geq$
 425 0.1 within 32 s are dominant in the peak of the butterfly distribution (Figure 6). It sug-
 426 gests the importance of individual scattering processes not exactly described in quasi-
 427 linear processes. Furthermore, a timescale (Δt) for a pitch angle change of an electron
 428 is different in each scattering and tends to be shorter than 200 ms (See timescales of t_w
 429 shown in Figure 8). Thus, the instantaneous pitch angle changes (D_{TP}) with $\Delta t = 200$
 430 ms tend to be underestimated here. We suggest that the contribution of the rapid scat-
 431 tering processes to the butterfly distribution is more important than our estimations. Lakhina
 432 et al. (2010) reported that instantaneously coherent chorus waves can realize a more rapid
 433 pitch angle scattering of electrons than that expected in quasi-linear models. The OFA
 434 spectrum (Figure 1) frequently shows relatively narrow frequency spectra, so the scat-
 435 tering process proposed by Lakhina et al. (2010) could work effectively. Moreover, when
 436 a wave amplitude of a narrow frequency spectra exceeds a certain threshold, phase trap-

437 ping/dislocation largely increases/decreases the pitch angle and energy of electrons, as
 438 shown in Figures 7 and 8. The pitch angle and energy transports by the phase trapping/dislocation
 439 show large D_{TP} of electrons, which contribute to the formation of the butterfly distri-
 440 bution. Recently, Gan, Li, Ma, Artemyev, and Albert (2020) have also reported the im-
 441 portance of nonlinear scattering in rapid electron acceleration at energies of tens of keV
 442 in terms of the formation of a butterfly distribution due to whistler chorus bursts. The
 443 scattering in instantaneously coherent chorus waves and the scattering by phase trap-
 444 ping/dislocation are not described as quasi-linear models. We expect that non-quasi-linear
 445 processes play an important role in forming a butterfly distribution of energetic electrons.
 446 Furthermore, the phase trapping process plays a more important role than the disloca-
 447 tion process, because the phase dislocation reduces the energy of electrons. The phase
 448 trapping would have a dominant contribution to the rapid acceleration of electrons that
 449 form the butterfly distribution at 24.5 keV.

450 In our simulation, there is no phase correlation among the wave modes, as described
 451 in Sec. 3.2. Usually, electrons are not easily trapped by broadband fluctuations with ran-
 452 dom wave phases. However, if there is an amplitude modulation in time and frequency,
 453 a particular wave mode can possibly be dominant. As a situation in which the wave mode
 454 that has $|S| \sim 1$ continues for a finite time, efficient acceleration associated with the
 455 phase trapping can occur even if there is no phase coherency with other wave modes with
 456 lower amplitudes.

457 The upper-band chorus burst used in the simulation is highly modulated in am-
 458 plitude (Figure 1). The wave amplitude in the burst intermittently exceeds 100 pT in
 459 a narrow frequency range of about 100 - 200 Hz. Thus, some electrons are phase-trapped
 460 and gain energy in a short duration owing to intermittently enhanced wave modes (Fig-
 461 ure 8). It is expected that the energy gain by the phase trapping is more efficient than
 462 the quasi-linear diffusion process even without a long-duration trapping (~ 1 sec.), as
 463 described by Omura et al. (2007). Recently, the important role of the phase trapping pro-
 464 cess in an amplitude-modulated whistler chorus wave has also been studied numerically
 465 by Hiraga and Omura (2020) and Gan, Li, Ma, Albert, et al. (2020). Our simulation and
 466 other numerical studies suggest the importance of considering realistic wave modes that
 467 contribute to electron accelerations. In quasi-linear diffusion models, statistical wave mod-
 468 els are utilized, which eliminate the contribution of the amplitude modulation by aver-
 469 aging in time. The model that takes averaged signatures of waves may underestimate

470 the acceleration of electrons by each of the whistler chorus bursts or elements. In the-
 471 theoretical and numerical studies, appropriate wave models should be chosen to reproduce
 472 transient energetic electron dynamics that are actually observed in the magnetosphere.

473 As seen in Figures 7 and 8, the electron scattering shows not only small energy changes
 474 but also large energy changes induced by phase trapping and dislocation. A scattering
 475 process can be evaluated using an instantaneous inhomogeneity ratio S defined in Equa-
 476 tion (8). The contribution of wave modes with $|S| \gg 1$ to electrons becomes dominant
 477 when the energy change is small, whereas that with $|S| < 1$ becomes dominant when
 478 the energy change is large (Figure 9). Larger wave amplitudes reduce $|S|$ because of the
 479 Ω_w^{-1} term, and the electron position also contributes to the reduction in $|S|$ because $|\partial\Omega_e/\partial s|$
 480 tends to be smaller at lower latitudes. Note that $\partial\Omega_e/\partial s$ at the electron position is pro-
 481 portional to the spatial gradient of the background magnetic field along its field line. An
 482 instantaneous change of an inhomogeneity factor leads to a variety of scattering processes
 483 for an electron in the upper-band chorus burst.

484 The wave model used in the RBW simulation shown in this paper has a frequency
 485 gap of 64 Hz among wave modes, and thus, it does not perfectly construct the incoher-
 486 ent wave burst as defined in a quasi-linear diffusion model. Moreover, the time resolu-
 487 tion of the wave model is limited to 1 s; thus, amplitude modulations shorter than 1 s
 488 are not reproduced. However, the simulation has demonstrated the Arase observations
 489 relatively well, implying that the observed upper-band whistler chorus burst may be close
 490 to the condition assumed in the wave model. That is, the observed burst might be co-
 491 herent with a finite frequency (of about 64 Hz) and the amplitude modulation might not
 492 be much shorter than 1 s. It is necessary to consider the actual wave form data of whistler
 493 chorus waves covering a longer time scale in order to reproduce the actual electron scat-
 494 tering processes in future simulations.

495 **6 Summary and conclusions**

496 We have performed a data-driven RBW simulation using Arase observations to study
 497 the rapid flux enhancement of energetic electrons with the upper-band whistler chorus
 498 burst in the duration of about 30 s. The simulation reproduces the temporal variation
 499 of the electron flux distribution observed by Arase. As a result of detailed analysis of
 500 the simulation data, it is found that 15 – 16 keV electrons with the equatorial pitch an-

501 gle of 40 – 50 degrees contribute to the flux enhancement at energies higher than 20 keV
502 at large pitch angles. We have found that scattering processes not described by the quasi-
503 linear diffusion model contribute to the electron acceleration that forms the butterfly dis-
504 tribution at 24.5 keV. Our simulation suggests that a time-averaged statistical wave model
505 as used in quasi-linear models underestimates the acceleration efficiency of radiation belt
506 electrons in each of the whistler chorus bursts and elements.

507 We conclude that the rapid flux enhancement of energetic electrons observed by
508 Arase is caused by the phase trapping of electrons associated with a highly amplitude-
509 modulated upper-band whistler chorus burst. It is also suggested that the contribution
510 of the amplitude modulation, which leads to the intermittent enhancement of the wave
511 amplitude, should be properly taken into account in wave models for theoretical and nu-
512 merical studies.

513 **Acknowledgments**

514 This work was supported by JSPS KAKENHI Grant Numbers JP15H05815 and JP20H01959.
515 Science data of the ERG (Arase) satellite were obtained from the ERG Science Center
516 (ERG-SC) operated by ISAS/JAXA and ISEE/Nagoya University ([https://ergsc.isee.nagoya-](https://ergsc.isee.nagoya-u.ac.jp/index.shtml.en)
517 [u.ac.jp/index.shtml.en](https://ergsc.isee.nagoya-u.ac.jp/index.shtml.en), Miyoshi, Hori, et al. (2018)). Part of the work of SK, YM, TH,
518 MS, SN, and SI was carried out at ERG-SC. In this study, we analyzed the MEP-e level
519 3 v1.01, MGF level 2 v1.02 and the PWE/OFA-SPEC level 2 v2.01. Arase MGF Level-
520 2 dataset used for this research is available in Matsuoka, Teramoto, Imajo, et al. (2018).

521 **References**

- 522 Albert, J. M. (1999). Analysis of quasi-linear diffusion coefficients. *Jour-*
523 *nal of Geophysical Research: Space Physics*, *104*(A2), 2429–2441. doi:
524 10.1029/1998JA900113
- 525 Bortnik, J., Thorne, R. M., & Inan, U. S. (2008). Nonlinear interaction of ener-
526 getic electrons with large amplitude chorus. *Geophysical Research Letters*, *35*,
527 L21102,. doi: 10.1029/2008GL035500
- 528 Bortnik, J., Thorne, R. M., & Meredith, N. P. (2007). Modeling the prop-
529 agation characteristics of chorus using CRRES suprathermal electron
530 fluxes. *Journal of Geophysical Research: Space Physics*, *112*, A08204. doi:
531 10.1029/2006JA012237

- 532 Branch, M. A., Coleman, T. F., & Li, Y. (1999). A Subspace, Interior, and
 533 Conjugate Gradient Method for Large-Scale Bound-Constrained Minimization
 534 Problems. *SIAM Journal on Scientific Computing*, *21*(1), 1–23. doi:
 535 10.1137/S1064827595289108
- 536 Buneman, O. (1993). *Computer space plasma physics: Simulation techniques and*
 537 *software* (H. Matsumoto & Y. Omura, Eds.). Terra Scientific Publishing
 538 Company (TERRAPUB). Retrieved from [https://www.terrapub.co.jp/](https://www.terrapub.co.jp/e-library/cspp/pdf/03.pdf)
 539 [e-library/cspp/pdf/03.pdf](https://www.terrapub.co.jp/e-library/cspp/pdf/03.pdf)
- 540 Fennell, J. F., Roeder, J. L., Kurth, W. S., Henderson, M. G., Larsen, B. A., Hospo-
 541 darsky, G., . . . Reeves, G. D. (2014). Van Allen Probes observations of direct
 542 wave-particle interactions. *Geophysical Research Letters*, *41*, 1869–1875. doi:
 543 10.1002/2013GL059165
- 544 Gan, L., Li, W., Ma, Q., Albert, J. M., Artemyev, A. V., & Bortnik, J. (2020).
 545 Nonlinear Interactions Between Radiation Belt Electrons and Chorus Waves:
 546 Dependence on Wave Amplitude Modulation. *Geophysical Research Letters*,
 547 *47*, e2019GL085987. doi: 10.1029/2019GL085987
- 548 Gan, L., Li, W., Ma, Q., Artemyev, A. V., & Albert, J. M. (2020). Unraveling
 549 the Formation Mechanism for the Bursts of Electron Butterfly Distributions:
 550 Test Particle and Quasilinear Simulations. *Geophysical Research Letters*, *47*,
 551 e2020GL090749. doi: 10.1029/2020GL090749
- 552 Glauert, S. A., Horne, R. B., & Meredith, N. P. (2014). Three-dimensional elec-
 553 tron radiation belt simulations using the BAS Radiation Belt Model with
 554 new diffusion models for chorus, plasmaspheric hiss, and lightning-generated
 555 whistlers. *Journal of Geophysical Research: Space Physics*, *119*, 268–289. doi:
 556 10.1002/2013JA019281
- 557 Hiraga, R., & Omura, Y. (2020). Acceleration mechanism of radiation belt elec-
 558 trons through interaction with multi-subpacket chorus waves. *Earth, Planets*
 559 *and Space*, *72*, 21. doi: 10.1186/s40623-020-1134-3
- 560 Horne, R. B., & Thorne, R. M. (2003). Relativistic electron acceleration and precipi-
 561 tation during resonant interactions with whistler-mode chorus. *Geophysical Re-*
 562 *search Letters*, *30*(10), 1527. doi: 10.1029/2003GL016973
- 563 Kasahara, S., Yokota, S., Mitani, T., Asamura, K., Hirahara, M., Shibano, Y., &
 564 Takashima, T. (2018). Medium-energy particle experiments?electron analyzer

- 565 (MEP-e) for the exploration of energization and radiation in geospace (ERG)
566 mission. *Earth, Planets and Space*, *70*, 69. doi: 10.1186/s40623-018-0847-z
- 567 Kasahara, Y., Kasaba, Y., Kojima, H., Yagitani, S., Ishisaka, K., Kumamoto,
568 A., ... Shinohara, I. (2018). The Plasma Wave Experiment (PWE) on
569 board the Arase (ERG) satellite. *Earth, Planets and Space*, *70*, 86. doi:
570 10.1186/s40623-018-0842-4
- 571 Kumamoto, A., Tsuchiya, F., Kasahara, Y., Kasaba, Y., Kojima, H., Yagitani, S.,
572 ... Obara, T. (2018). High Frequency Analyzer (HFA) of Plasma Wave Exper-
573 iment (PWE) onboard the Arase spacecraft. *Earth, Planets and Space*, *70*, 82.
574 doi: 10.1186/s40623-018-0854-0
- 575 Kurita, S., Miyoshi, Y., Kasahara, S., Yokota, S., Kasahara, Y., Matsuda, S., ...
576 Shinohara, I. (2018). Deformation of Electron Pitch Angle Distributions
577 Caused by Upper Band Chorus Observed by the Arase Satellite. *Geophysical*
578 *Research Letters*, *45*, 7996–8004. doi: 10.1029/2018GL079104
- 579 Lakhina, G. S., Tsurutani, B. T., Verkhoglyadova, O. P., & Pickett, J. S. (2010).
580 Pitch angle transport of electrons due to cyclotron interactions with the coher-
581 ent chorus subelements. *Journal of Geophysical Research: Space Physics*, *115*,
582 A00F15. doi: 10.1029/2009JA014885
- 583 Matsuda, S., Kasahara, Y., Kojima, H., Kasaba, Y., Yagitani, S., Ozaki, M., ... Shi-
584 nohara, I. (2018). Onboard software of Plasma Wave Experiment aboard
585 Arase: instrument management and signal processing of Waveform Cap-
586 ture/Onboard Frequency Analyzer. *Earth, Planets and Space*, *70*, 75. doi:
587 10.1186/s40623-018-0838-0
- 588 Matsuoka, A., Teramoto, M., Imajo, S., Kurita, S., Miyoshi, Y., & Shinohara, I.
589 (2018). updated daily. The MGF instrument Level-2 spin-fit magnetic field
590 data of Exploration of energization and Radiation in Geospace (ERG) Arase
591 satellite, Version v01.02. ERG Science Center, Institute for Space-Earth En-
592 vironmental Research, Nagoya University. doi: 10.34515/DATA.ERG-06001
593 Accessed 2020-11-06.
- 594 Matsuoka, A., Teramoto, M., Nomura, R., Nosé, M., Fujimoto, A., Tanaka, Y., ...
595 Shinohara, I. (2018). The ARASE (ERG) magnetic field investigation. *Earth,*
596 *Planets and Space*, *70*, 43. doi: 10.1186/s40623-018-0800-1
- 597 Miyoshi, Y., Hori, T., Shoji, M., Teramoto, M., Chang, T. F., Segawa, T., ... Shino-

- 598 hara, I. (2018). The ERG Science Center. *Earth, Planets and Space*, *70*, 96.
599 doi: 10.1186/s40623-018-0867-8
- 600 Miyoshi, Y., Kataoka, R., Kasahara, Y., Kumamoto, A., Nagai, T., & Thomsen,
601 M. F. (2013). High-speed solar wind with southward interplanetary magnetic
602 field causes relativistic electron flux enhancement of the outer radiation belt
603 via enhanced condition of whistler waves. *Geophysical Research Letters*, *40*,
604 4520–4525. doi: 10.1002/grl.50916
- 605 Miyoshi, Y., Morioka, A., Misawa, H., Obara, T., Nagai, T., & Kasahara, Y. (2003).
606 Rebuilding process of the outer radiation belt during the 3 November 1993
607 magnetic storm: NOAA and Exos-D observations. *Journal of Geophysical
608 Research: Space Physics*, *108*(A1), 1004. doi: 10.1029/2001JA007542
- 609 Miyoshi, Y., Oyama, S., Saito, S., Kurita, S., Fujiwara, H., Kataoka, R., ...
610 Tsuchiya, F. (2015). Energetic electron precipitation associated with pulsating
611 aurora: EISCAT and Van Allen Probe observations. *Journal of Geophysical
612 Research: Space Physics*, *120*, 2754–2766. doi: 10.1002/2014JA020690
- 613 Miyoshi, Y., Saito, S., Kurita, S., Asamura, K., Hosokawa, K., Sakanoi, T., ...
614 Blake, J. B. (2020). Relativistic Electron Microbursts as High Energy Tail of
615 Pulsating Aurora Electrons. *Geophysical Research Letters*, *47*, e2020GL090360.
616 doi: 10.1029/2020GL090360
- 617 Miyoshi, Y., Saito, S., Seki, K., Nishiyama, T., Kataoka, R., Asamura, K., ...
618 Santolik, O. (2015). Relation between fine structure of energy spectra for
619 pulsating aurora electrons and frequency spectra of whistler mode chorus
620 waves. *Journal of Geophysical Research: Space Physics*, *120*, 7728–7736. doi:
621 10.1002/2015JA021562
- 622 Miyoshi, Y., Shinohara, I., Takashima, T., Asamura, K., Higashio, N., Mitani, T., ...
623 Seki, K. (2018). Geospace exploration project ERG. *Earth, Planets and Space*,
624 *70*, 101. doi: 10.1186/s40623-018-0862-0
- 625 Omura, Y., Furuya, N., & Summers, D. (2007). Relativistic turning acceleration
626 of resonant electrons by coherent whistler mode waves in a dipole magnetic
627 field. *Journal of Geophysical Research: Space Physics*, *112*, A06236. doi:
628 10.1029/2006JA012243
- 629 Saito, S., Miyoshi, Y., & Seki, K. (2012). Relativistic electron microbursts as-
630 sociated with whistler chorus rising tone elements: GEMSIS-RBW simula-

- 631 tions. *Journal of Geophysical Research: Space Physics*, *117*, A10206. doi:
632 10.1029/2012JA018020
- 633 Saito, S., Miyoshi, Y., & Seki, K. (2016). Rapid increase in relativistic electron
634 flux controlled by nonlinear phase trapping of whistler chorus elements.
635 *Journal of Geophysical Research: Space Physics*, *121*, 6573–6589. doi:
636 10.1002/2016JA022696
- 637 Santolík, O., Parrot, M., & Lefeuvre, F. (2003). Singular value decomposition meth-
638 ods for wave propagation analysis. *Radio Science*, *38*, 1010. doi: 10.1029/
639 2000RS002523
- 640 Thorne, R. M., Li, W., Ni, B., Ma, Q., Bortnik, J., Chen, L., ... Kanekal, S. G.
641 (2013). Rapid local acceleration of relativistic radiation-belt electrons by
642 magnetospheric chorus. *Nature*, *504*, 411–414. doi: 10.1038/nature12889
- 643 Tsurutani, B. T., & Smith, E. J. (1977). Two types of magnetospheric ELF chorus
644 and their substorm dependences. *Journal of Geophysical Research (1896-1977)*,
645 *82*(32), 5112–5128. doi: 10.1029/JA082i032p05112
- 646 Tu, W., Cunningham, G. S., Chen, Y., Morley, S. K., Reeves, G. D., Blake, J. B.,
647 ... Spence, H. (2014). Event-specific chorus wave and electron seed popula-
648 tion models in DREAM3D using the Van Allen Probes. *Geophysical Research*
649 *Letters*, *41*, 1359–1366. doi: 10.1002/2013GL058819
- 650 Virtanen, P., Gommers, R., Oliphant, T. E., Haberland, M., Reddy, T., Cournau-
651 peau, D., ... Contributors, S. ... (2020). SciPy 1.0: Fundamental Algorithms
652 for Scientific Computing in Python. *Nature Methods*, *17*, 261–272. doi:
653 <https://doi.org/10.1038/s41592-019-0686-2>